

# Discriminating physical and non-physical diffracted energy in source–receiver interferometry

Giovanni Angelo Meles and Andrew Curtis

*School of Geosciences, University of Edinburgh, West Mains Road, Edinburgh EH9 3JW, UK. E-mail: gmeles@staffmail.ed.ac.uk*

Accepted 2014 February 11. Received 2014 January 8; in original form 2013 June 29

## SUMMARY

We show how physical and non-physical diffracted waves can be discriminated in source–receiver interferometry (SRI), a wavefield interferometric method that constructs Green's functions between any source–receiver pair. These can be estimated by convolution and cross-correlation of wavefields propagating to or from other sources or receivers. SRI has been observed to work surprisingly well in practical applications when theoretical requirements (e.g. complete enclosing boundaries of other sources and receivers) are contravened as is standard in practical applications. As a partial explanation to this, it has been demonstrated previously that SRI for single diffractor problems produces correct Green's functions estimates without requiring wavefields to be generated around specific stationary-phase points in space (as is required by other forms of interferometry). In this paper, we show that also for multiple-diffractor problems, any boundary source–receiver pair produces stationary, correct kinematics for singly and multiply diffracted waves. However, when multiple diffractors are present, non-physical artefacts are produced in Green's functions estimated by SRI with incomplete boundaries. We introduce a purely data-driven algorithm that allows traveltimes of any order of physical, diffracted waves to be predicted. This reduces ambiguity in interpreting wavefields generated using SRI with only partial boundaries: this also permits spurious or non-physical energy in the constructed Green's functions to be identified and either interpreted or ignored.

**Key words:** Interferometry; Wave scattering and diffraction; Wave propagation; Acoustic properties.

## INTRODUCTION

Seismic interferometry generally refers to any technique that allows the construction or synthesis of Green's functions between two locations by means of integration of the cross-correlation or convolution of other wavefields (Claerbout 1968; Rickett & Claerbout 1999; Wapenaar & Fokkema 2006). Depending on the recording configuration, we distinguish between interreceiver (Campillo & Paul 2003; Wapenaar 2004), intersource (Hong & Menke 2006; Curtis *et al.* 2009) and source–receiver (Curtis & Halliday 2010) interferometry. Each refers to whether sources or receivers occupy the locations between which interferometry constructs the Green's function (Fig. 1). This paper examines how diffracted or scattered energy is redistributed during seismic interferometry.

Diffracted waves are created when an incident wavefield interacts with structures of small spatial extent relative to the wavelength. The resulting re-distribution of wave energy is often called *scattering*. In geophysics, for example, scattering may be caused by seismic waves interacting with subsurface angular boundaries between rocks of different elastic parameters or density, and embedded scatterers may be formed by voids (e.g. caves) or faults and fractures. Identification and location of such features helps in the interpretation of seismic data.

The potential advantages of using diffracted waves have been studied in a diversity of fields since the seminal works of Krey (1952) and Hagedoorn (1954). More recently, algorithms were designed to discriminate between reflected and diffracted waves (Landa *et al.* 1987), and similar approaches were used to perform high-resolution investigation of the Earth's subsurface using ground penetrating radar data (Papziner & Nick 1998), and to analyse the benefit of employing low-amplitude diffracted energy for seismic imaging (Neidell 1997). Diffracted arrivals also help in the identification of geological strata that have particularly strong internal heterogeneity such as karstic carbonates (Grasmueck *et al.* 2012).

Within the field of interferometry, scattering has been studied in the context of standard interreceiver (Vasconcelos *et al.* 2009; Snieder & Fleury 2010; Wapenaar *et al.* 2010) and source–receiver interferometry (SRI: Halliday & Curtis 2010; Poliannikov 2011; Vasconcelos 2011; Poliannikov & Ling 2012). Experimental evidence (Duguid *et al.* 2011; Curtis *et al.* 2012) and theoretical insights (Bharadwaj *et al.* 2011;

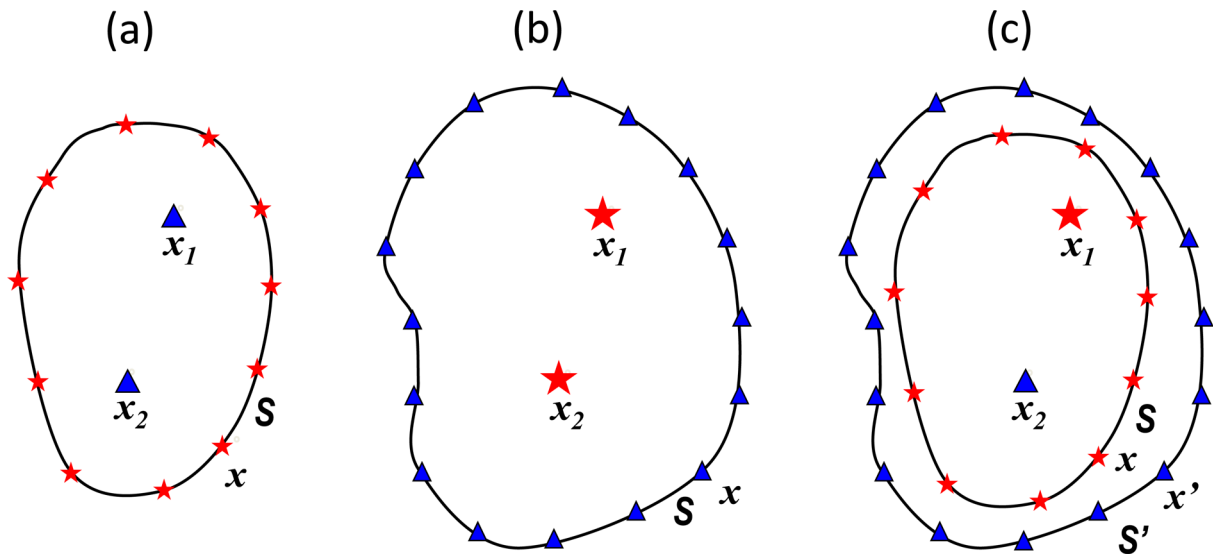


**Figure 1.** Geometrical configuration for (a) interreceiver, (b) intersource and (c) source–receiver interferometry. Triangles and stars represent receivers and sources, respectively. Locations  $x$  and  $x'$  are on closed surfaces  $S$  and  $S'$ , respectively. Interferometry constructs the Green's function between  $x_1$  and  $x_2$  in each case.

Poliannikov 2011; King & Curtis 2012) suggest that SRI may be more robust than some other forms of interferometry with respect to violation in practical experiments of the theoretical geometrical requirements such as completeness of the boundaries in Fig. 1. More precisely, the artefacts in Green's functions reconstructions due to incomplete boundaries or other common approximations (usually referred to as non-physical or spurious energy) exhibit lower amplitudes when SRI is employed as an alternative to interreceiver interferometry. SRI has been shown to be equivalent to a two-step procedure (Curtis *et al.* 2012) involving subsequent applications of standard interreceiver (turning the internal receiver  $x_2$  in Fig. 1c into a virtual source) and intersource interferometry (between  $x_1$  and  $x_2$  in Fig. 1c). For the single scattering problem, it was shown that in the second step of SRI, non-physical results from the first interreceiver step of SRI are transformed into waves that emulate physical energy (Meles & Curtis 2013a); King & Curtis (2012) showed a similar result for reflected waves, and Bharadwaj *et al.* (2011) for refracted waves.

In this paper, we first present a method to classify diffractors based on the variation of acoustic wave traveltime variations (their so-called *moveouts*) across source and receiver arrays, which results in a practical method to 'fingerprint' individual diffractors in multiple-scattering scenarios. We then analyse multiple-scattering problems of purely diffracted waves, for which we derive stationary phase conditions for both physical and so-called non-physical energy in SRI. Finally, we show how fingerprints can be used to predict traveltimes of any singly and multiply scattered waves, allowing physical and non-physical energy to be discriminated in source–receiver interferometric Green's functions estimates.

## FINGERPRINTING INDIVIDUAL DIFFRACTORS

A basic geometrical property of all waves scattered last at a certain diffractor is that their moveout across an array of receivers is invariant (Khaidukov *et al.* 2004). In other words, either moving the source or following a different scattering path prior to arriving at the last scatterer can only affect the constant (lag) component of diffracted arrival times observed across any array of receivers, but not their variation or moveout across the array (Fig. 2). This property holds irrespective of the complexity of the medium, and can be demonstrated rigorously by analysing the fully non-linear Lippmann Schwinger equation for perturbed media (Meles & Curtis 2013b). This characteristic of scattered waves can be used in multisource data acquisition to identify and remove diffraction components, to enhance the scattered wave signals by removing reflected and refracted waves, and to identify edge diffraction signals (Klem-Musatov 1994). By reciprocity, moveout of waves scattered first at a certain diffractor across a source array is invariant with respect to receiver position, or to the subsequent scattering path. In addition, each scatterer exhibits a different moveout across source and receiver arrays. Other than for pathological situations, for example, where scatterers are located exactly symmetrically with respect to receivers arrays, each scatterer can therefore be 'fingerprinted', or tagged, uniquely by their specific moveout, without knowing the scatterers' locations. In the following, we discuss how this simple property is sufficient to predict any multiply scattered wave traveltime in SRI.

## IDENTIFYING FIRST AND LAST DIFFRACTORS

Meles & Curtis (2013b) showed how any observed multiply diffracted wave can be decomposed into a series of ordered single scattering events. Since we draw on that theory, we summarize the relevant parts here.

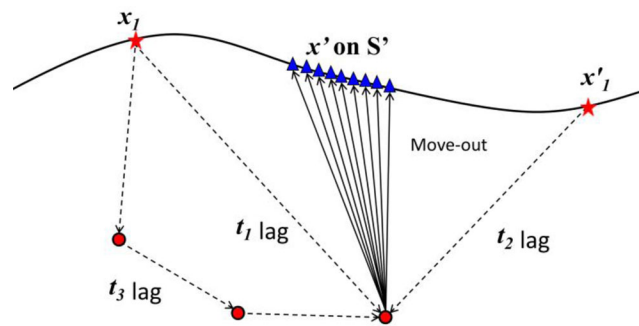


**Figure 2.** Scattered wave ray paths. Stars and triangles are sources and receivers, respectively, and red circles are scatterers. The receiver array moveout associated with scattered waves does not depend on the position of the source since the relative traveltime variations to different receivers are controlled by the distance between the final scatterer and the receivers (solid rays). The traveltime between the source and the scatterer (dashed rays) only changes the constant component of traveltimes across the array (the  $t_1$ ,  $t_2$  or  $t_3$  lag due to different source positions or scattering paths).

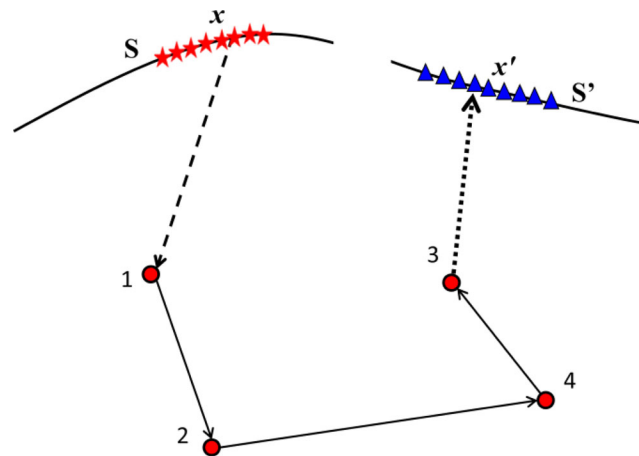


**Figure 3.** Any multiply scattered wave can be divided into three-component paths: the source-to-first-scatterer (dashed line), the interscatterer path (solid line) and the last-scatterer-to-receiver path (dotted line). The complexity of the interscatterer component (which may also have zero length for a singly scattered wave) does not affect the simplicity of the first and third components. Key as in Fig. 2.

When multiple diffractors are embedded within an otherwise homogeneous medium, measured seismograms record direct (non-scattered), singly scattered (herein, by this we mean energy that only interacts with one diffractor), and multiply scattered (energy that interacts with more than one diffractor) waves. Despite their complexity, these multiply scattered wavefields can always be decomposed into three paths (see Fig. 3): a first connecting the source to the first diffractor (dashed line in Fig. 3), a second connecting all of the diffractors involved (solid line in Fig. 3) and a third connecting the last diffractor to the receiver (dotted line in Fig. 3). Notwithstanding the potential complexity of the interdiffractor component, the possible number of combinations for the first and third of these paths is limited and equal to the number of diffractors.

Since each and every diffracted wave has a first and last diffractor (which may coincide in the case of first-order scattering), in principle, a classification of all scattered waves can be made based on this information. In order to be useful for the analysis of real wavefields, however, this classification needs to be identifiable from recorded data. We now show how this can be achieved.

Say a source is fired at  $x$ , a point on surface  $S$  and waveform recordings are acquired at receivers  $x'$  along surface  $S'$ , where  $S$  and  $S'$  may differ (Fig. 4a). Among the many scattering combinations, two paths are shown (solid and dashed lines in Fig. 4a). Both paths have last diffractor 4, and therefore exhibit identical moveout across the receiver array (the moveout of the wide arrows in Fig. 4a). All waves scattered last at scatterer 4 will share this moveout, and only in pathological cases would any other wave share this moveout. Thus, all waves scattered last at scatterer 4 can be identified and classified as such. A similar classification can be made for every other last scatterer. As a result, in the case that the distribution of receivers on  $S'$  is dense enough to identify the moveouts of each diffractor without ambiguity, any observed scattered wave can be classified according to its last diffractor. By reciprocity, a similar argument holds for moveout across the source array on  $S$ , and the *first* diffractor of any scattered wave can always be identified (Fig. 4b). It is important to note here that the means by which each first and last diffractor is identified is exactly by matching the moveout—the fingerprint or tag—of that diffractor, as introduced in the previous section.

While the above methodology assumes for simplicity that all of the relevant scattered energy is due to diffractors, the classification based on finger prints extends to more general situations. In the derivation of the expression of the scattered field in the Lipmann–Schwinger equation, no assumption is made about the background model. As a consequence, this system of classification also extends to non-isotropic scatterers embedded in inhomogeneous background media (Meles & Curtis 2013b). It therefore begins to decompose the complexity of wavefields associated with quite a general class of multiple-scattering problems into readily identifiable subcomponents.

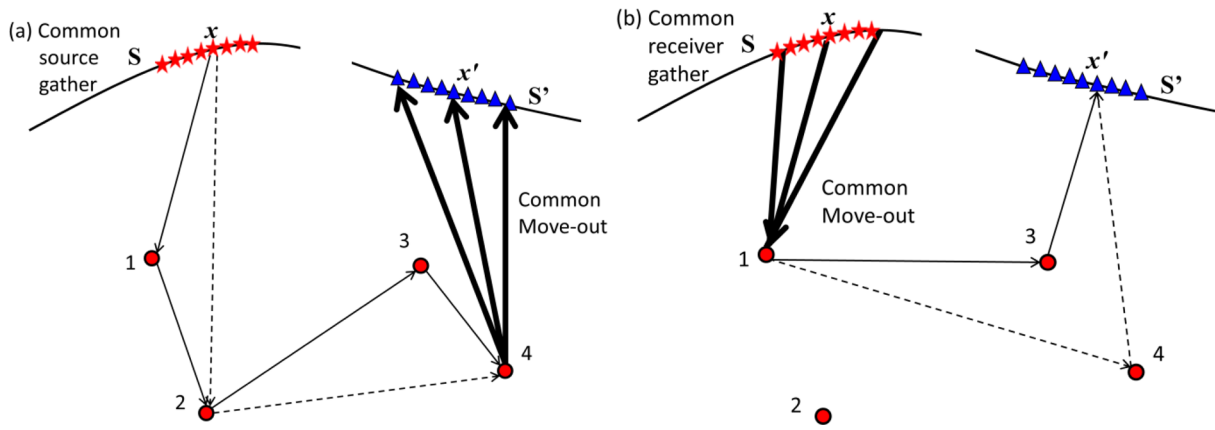


**Figure 4.** (a) A fixed source is fired at position  $x$  in surface  $S$ , and the corresponding wavefield is recorded by receivers at  $x'$  within surface  $S'$ . Moveouts across the receiver array  $S'$  only depend on the path connecting the last scatterer to the receivers since for every individual scattered wave, the section of the path up to the last scatterer remains fixed for a given observed moveout of the thick arrows. Arrivals that share identical last scatterer (solid and dashed paths) therefore exhibit the same receiver array moveout. (b) As for (a), but for a fixed receiver: waves that share an identical first scatterer exhibit the same source array moveout (thick arrows). Key as in Fig. 2.

## SCATTERING IN SRI

For acoustic media and geometries represented schematically in Fig. 1(a), frequency-domain interreceiver interferometry allows the sum of any Green's function and its complex conjugate (together known as the homogenous Green's function) between two receiver locations to be expressed in the frequency domain as (van Manen *et al.* 2005; Wapenaar & Fokkema 2006):

$$G(x_2, x_1) + G^*(x_2, x_1) = \frac{-1}{j\omega\rho} \int_S \{G^*(x_2, x)n_i\partial_i G(x_1, x) - n_i\partial_i G^*(x_2, x)G(x_1, x)\} dS. \quad (1)$$

Here,  $j$  is the imaginary unit,  $\rho$  denotes the medium density,  $x_1$  and  $x_2$  indicate receiver positions,  $G(x_2, x_1)$  represents the Green's function recorded at  $x_2$  for an impulsive source at  $x_1$ ,  $S$  stands for an arbitrary source boundary enclosing  $x_1$  and  $x_2$ , and  $n_i$  and  $\partial_i$  represent the  $i$ th cartesian component of the normal vector to  $S$  and of the gradient, respectively. Einstein summation over repeated indices is used here as in all of the following equations.

Eq. (1) assumes constant density. Heterogeneous density distributions may be represented by simply moving  $-1/j\omega\rho$  inside the integral. However, eq. (1) is exact for an arbitrary velocity distribution even though there is no explicit dependence on velocity—its effects are accounted for implicitly within the various Green's functions.

Intersource interferometry, which provides a method to compute the Green's function between two sources surrounded by a closed boundary of receivers (Fig. 1b), follows most directly by applying source–receiver reciprocity to interreceiver interferometry theory (Curtis *et al.* 2009). Combined application of interreceiver and intersource interferometry allows the homogeneous Green's function between a source and a receiver to be expressed as a double surface integral, the result being known as source–receiver interferometry or SRI (Curtis 2009; Curtis & Halliday 2010). In the acoustic case, for the geometry in Fig. 1(c), this result is expressed as

$$G(x_2, x_1) + G^*(x_2, x_1) = \frac{-1}{j\omega\rho} \int_S \left\{ \left[ \frac{1}{j\omega\rho} \int_{S'} \{G(x', x_1)n_{i'}\partial_{i'} G^*(x', x) - n_{i'}\partial_{i'} G(x', x_1)G^*(x', x)\} dS' \right] n_i \partial_i G(x_2, x) \right. \\ \left. - \partial_i n_i \left[ \frac{1}{j\omega\rho} \int_{S'} \{G(x', x_1)n_{i'}\partial_{i'} G^*(x', x) - n_{i'}\partial_{i'} G(x', x_1)G^*(x', x)\} dS' \right] G(x_2, x) \right\} dS. \quad (2)$$

In SRI,  $x_1$  and  $x_2$  usually indicate source and receiver positions, respectively, while  $S'$  stands for an arbitrary receiver boundary enclosing all of  $S$ ,  $x_1$  and  $x_2$ . Curtis & Halliday (2010) give equivalent expressions for a variety of canonical geometries, and for elastic media.

SRI allows the homogeneous Green's function between a source and a receiver to be expressed as a double surface integral involving trilinear operators (Meles & Curtis 2013a)

$$G(x_2, x_1) + G^*(x_2, x_1) = \mathcal{L}[G_{x',x_1}; G_{x',x}; G_{x_2,x}], \quad (3)$$

$$G(x_2, x_1) + G^*(x_2, x_1) \approx \mathcal{L}^A[G_{x',x_1}; G_{x',x}; G_{x_2,x}], \quad (4)$$

where for acoustic media, we have (Curtis & Halliday 2010)

$$\begin{aligned} \mathfrak{L}[G_{x',x_1}; G_{x',x}; G_{x_2,x}] = & \frac{-1}{j\omega\rho} \int_S \left\{ \left[ \frac{1}{j\omega\rho} \int_{S'} \{G(x', x_1)n_{i'}\partial_{i'}G^*(x', x) - n_{i'}\partial_{i'}G(x', x_1)G^*(x', x)\} dS' \right] n_i \partial_i G(x_2, x) \right. \\ & \left. - \partial_i n_i \left[ \frac{1}{j\omega\rho} \int_{S'} \{G(x', x_1)n_{i'}\partial_{i'}G^*(x', x) - n_{i'}\partial_{i'}G(x', x_1)G^*(x', x)\} dS' \right] G(x_2, x) \right\} dS, \end{aligned} \quad (5)$$

and

$$\mathfrak{L}^A[G_{x',x_1}; G_{x',x}; G_{x_2,x}] = \frac{4k^2}{(\omega\rho)^2} \int_S \int_{S'} G(x', x_1)G^*(x', x)G(x_2, x)dS'dS, \quad (6)$$

and within the trilinear operators we use the notation  $G_{x',x} = G(x', x)$  for compactness. The approximation employed in eqs (4) and (6) assumes the high-frequency regime that receivers are in the far-field with respect to sources, and that outgoing waves travel approximately perpendicularly to boundaries  $S$  and  $S'$  (Wapenaar & Fokkema 2006).

To analyse scattering problems, it is often convenient to decompose all Green's functions into a background component  $G^0$  from a known reference or background of the medium, and a scattered wave component  $G^S$  resulting from a perturbation to the background medium's compressibility distribution:

$$G = G^0 + G^S. \quad (7)$$

If we substitute eq. (7) into eqs (5) and (6), due to the trilinearity of operators  $\mathfrak{L}$  and  $\mathfrak{L}^A$ , we obtain

$$\begin{aligned} G(x_2, x_1) + G^S(x_2, x_1) = & \mathfrak{L}[G_{x',x_1}^0; G_{x',x}^0; G_{x_2,x}^0] + \mathfrak{L}[G_{x',x_1}^0; G_{x',x}^S; G_{x_2,x}^0] + \mathfrak{L}[G_{x',x_1}^0; G_{x',x}^S; G_{x_2,x}^S] \\ & + \mathfrak{L}[G_{x',x_1}^0; G_{x',x}^0; G_{x_2,x}^S] + \mathfrak{L}[G_{x',x_1}^S; G_{x',x}^0; G_{x_2,x}^0] + \mathfrak{L}[G_{x',x_1}^S; G_{x',x}^0; G_{x_2,x}^S] \\ & + \mathfrak{L}[G_{x',x_1}^S; G_{x',x}^S; G_{x_2,x}^0] + \mathfrak{L}[G_{x',x_1}^S; G_{x',x}^S; G_{x_2,x}^S] \end{aligned} \quad (8)$$

$$\begin{aligned} \approx & \mathfrak{L}^A[G_{x',x_1}^0; G_{x',x}^0; G_{x_2,x}^0] + \mathfrak{L}^A[G_{x',x_1}^0; G_{x',x}^S; G_{x_2,x}^0] + \mathfrak{L}^A[G_{x',x_1}^0; G_{x',x}^S; G_{x_2,x}^S] \\ & + \mathfrak{L}^A[G_{x',x_1}^0; G_{x',x}^0; G_{x_2,x}^S] + \mathfrak{L}^A[G_{x',x_1}^S; G_{x',x}^0; G_{x_2,x}^0] + \mathfrak{L}^A[G_{x',x_1}^S; G_{x',x}^0; G_{x_2,x}^S] \\ & + \mathfrak{L}^A[G_{x',x_1}^S; G_{x',x}^S; G_{x_2,x}^0] + \mathfrak{L}^A[G_{x',x_1}^S; G_{x',x}^S; G_{x_2,x}^S]. \end{aligned} \quad (9)$$

An expression for the scattered field alone involving only surface integrals can then be obtained by cancelling purely  $G^0$  terms:

$$\begin{aligned} G^S(x_2, x_1) + G^{S^*}(x_2, x_1) = & \mathfrak{L}[G_{x',x_1}^0; G_{x',x}^S; G_{x_2,x}^0] + \mathfrak{L}[G_{x',x_1}^0; G_{x',x}^S; G_{x_2,x}^S] + \mathfrak{L}[G_{x',x_1}^0; G_{x',x}^0; G_{x_2,x}^S] + \mathfrak{L}[G_{x',x_1}^S; G_{x',x}^0; G_{x_2,x}^0] \\ & + \mathfrak{L}[G_{x',x_1}^S; G_{x',x}^0; G_{x_2,x}^S] + \mathfrak{L}[G_{x',x_1}^S; G_{x',x}^S; G_{x_2,x}^0] + \mathfrak{L}[G_{x',x_1}^S; G_{x',x}^S; G_{x_2,x}^S] \end{aligned} \quad (10)$$

$$\begin{aligned} \approx & \mathfrak{L}^A[G_{x',x_1}^0; G_{x',x}^S; G_{x_2,x}^0] + \mathfrak{L}^A[G_{x',x_1}^0; G_{x',x}^S; G_{x_2,x}^S] + \mathfrak{L}^A[G_{x',x_1}^0; G_{x',x}^0; G_{x_2,x}^S] + \mathfrak{L}^A[G_{x',x_1}^S; G_{x',x}^0; G_{x_2,x}^0] \\ & + \mathfrak{L}^A[G_{x',x_1}^S; G_{x',x}^0; G_{x_2,x}^S] + \mathfrak{L}^A[G_{x',x_1}^S; G_{x',x}^S; G_{x_2,x}^0] + \mathfrak{L}^A[G_{x',x_1}^S; G_{x',x}^S; G_{x_2,x}^S]. \end{aligned} \quad (11)$$

Eqs (10) and (11) provide fully non-linear expressions for any scattering perturbation. In the following, however, we focus only on diffraction problems, for which specific properties hold.

## DISCRIMINATING PHYSICAL ENERGY IN WAVEFIELD INTERFEROMETRY

In previous work, we have used eqs (10) and (11) to study single-point diffractor problems (Meles & Curtis 2013a), focusing in part on interesting properties of the term  $\mathfrak{L}^A[G_{x',x_1}^S; G_{x',x}^S; G_{x_2,x}^S]$  which only has scattered wave arguments. That work shows that with only a single scatterer present, this term always produces excellent approximations to physical energy in  $G^S(x_2, x_1)$ , and that reconstructions of singly scattered wavefields can therefore be obtained from the above equations by using *only* this term, even with very limited source and receiver boundary segments  $S$  and  $S'$  in place of the complete boundaries required by the full theory above and shown in Fig. 1. This result (which has no analogue in interreceiver or intersource interferometry) holds for the single scatterer problem because the integrand of  $\mathfrak{L}^A[G_{x',x_1}^S; G_{x',x}^S; G_{x_2,x}^S]$  (i.e.  $G^S(x', x_1)G^S(x_2, x)G^{S^*}(x', x)$  in the standard notation of eq. 6) is stationary with respect to  $x$  and  $x'$  for *any* source–receiver pair on boundaries  $S$  and  $S'$  (see Fig. 5), respectively, and for isotropic scatterers produces dynamically correct energy in the integral that corresponds closely to that of the physically scattered wave  $G^S(x_2, x_1)$ . This result, which is strictly valid for isotropic point scatterers (Løer *et al.* 2014; Meles & Curtis 2013a), is important because when surfaces  $S$  and  $S'$  are limited, as in most practical cases, there is no other existing way to discriminate

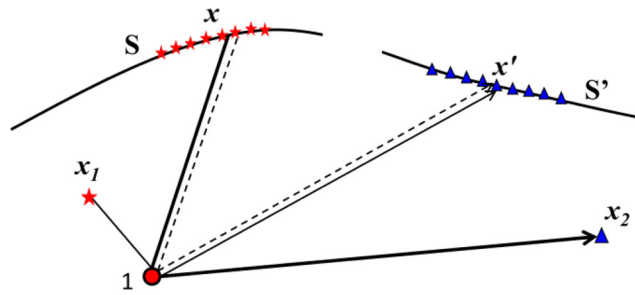


**Figure 5.** Construction of correct, singly scattered traveltimes in source–receiver interferometry with a single scatterer. The thin and thick solid lines stand for the convolved waves,  $G^S(x', x_1)$  and  $G^S(x_2, x)$ , respectively, while the dashed line indicates the cross-correlated event,  $G^S(x', x)$ .

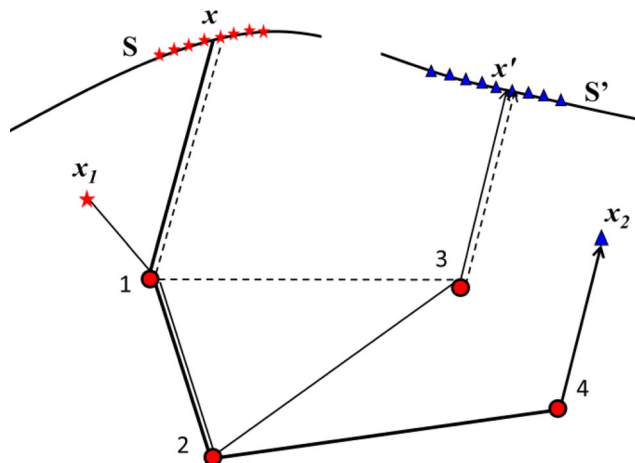
physical energy constructed by interferometry from non-physical energy (the latter resulting from errors due to the incompleteness of  $S$  and  $S'$ ). However, their results only hold for singly scattered waves and point diffractors. We extend here their analysis to the multiple-diffractors problem.

Will show in this paper that a proper combination of  $G^S(x', x)$ ,  $G^S(x_2, x)$  and  $G^S(x', x_1)$  can, in principle, provide all of the correct traveltime information about the causal, scattered, physical events of  $G^S(x_2, x_1)$  constructed from SRI, even when multiple diffractors are present. Due to the increased complexity of the problem, some care needs to be taken to avoid spurious (non-physical) waves from contaminating the constructed  $G^S(x_2, x_1)$ . However, as long as due attention is paid to the selection of scattered waves to be employed, this new algorithm allows us to differentiate true physical energy from spurious or non-physical energy in interferometric constructions of Green's functions when using incomplete boundaries  $S$  and  $S'$  in multiply scattering media (Snieder *et al.* 2006; King & Curtis 2012).

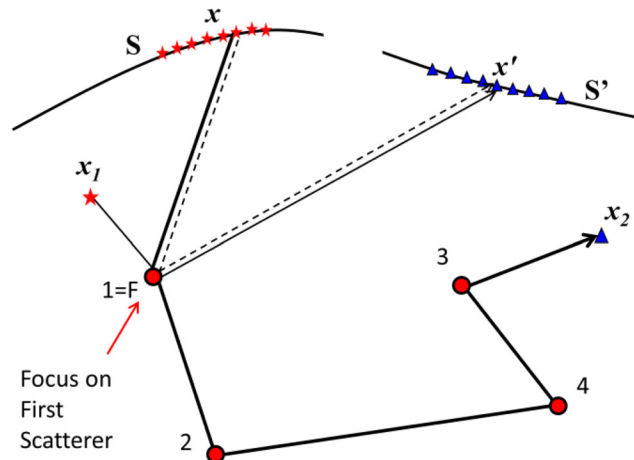
We first show that non-physical events can be associated with combinations of scattered waves when multiple diffractors are present. We then discuss a procedure using the theory above that allows the discrimination of physical from non-physical or spurious energy in the evaluation of  $\mathcal{L}^A[G_{x',x_1}^S, G_{x',x}^S, G_{x_2,x}^S]$ . We present numerical results to support our conclusions. As long as the ray approximation is reasonable, the results generalize to the case where the exact interferometric operator  $\mathcal{L}[G_{x',x_1}; G_{x',x}; G_{x_2,x}]$  is used in place of  $\mathcal{L}^A[G_{x',x_1}^S, G_{x',x}^S, G_{x_2,x}^S]$ , as the various terms in the former operator involve the same kinematics as individual terms in the latter (Meles & Curtis 2013a).

Fig. 5 shows a sketch representing the single diffractor case. For any source–receiver pair  $(x, x')$ , the combination of wavefields prescribed by the term  $\mathcal{L}^A[G_{x',x_1}^S, G_{x',x}^S, G_{x_2,x}^S]$  results in an event with a stationary phase that corresponds to that of the physical event  $G^S(x_2, x_1)$ . This can be seen to hold true because for any point pair  $(x', x)$  on boundary segments  $S$  and  $S'$ , application of the interferometric operator  $\mathcal{L}^A[G_{x',x_1}^S, G_{x',x}^S, G_{x_2,x}^S]$  results in cancellation (through cross-correlation) of traveltimes along common paths [1-to- $x'$ ] and [ $x$ -to-1] of  $G^S(x', x_1)$ ,  $G^S(x_2, x)$  and  $G^S(x', x)$  and the summation (through convolution) of traveltimes from [ $x_1$ -to-1] and [1-to- $x_2$ ]—eq. (6) (Meles & Curtis 2013a). This is because cross-correlation subtracts the phases of the correlated waves, while convolution adds the phases. Moreover, it has been shown dynamically that  $\mathcal{L}^A[G_{x',x_1}^S, G_{x',x}^S, G_{x_2,x}^S]$  provides an excellent proxy for the amplitudes or waveforms of  $G^S(x_2, x_1)$  (Löer *et al.* 2014; Meles & Curtis 2013a).

The situation is different when multiple scattering takes place. In Fig. 6, the construction of a stationary but non-physical phase is shown. Stationarity with respect to  $x$  and  $x'$  is attained whenever the ray paths connecting scatterers to sources  $x$  or receivers  $x'$  are shared by the three wavefields  $G^S(x', x_1)$ ,  $G^S(x_2, x)$  and  $G^{S*}(x', x)$ . More precisely, cancellation of common paths [3-to- $x'$ ] and [ $x$ -to-1] leads to stationarity with respect to  $x$  and  $x'$ , but the corresponding traveltime is artefactual, since it is the scattered traveltime from [ $x_1$ -to- $x_2$ ] plus the scattered traveltime from [1-to-2-to-3] minus the direct traveltime from [1-to-3]. This does not correspond to the traveltime of any physically possible wave path between  $x_1$  and  $x_2$ . The thin and thick solid lines stand for the convolved waves,  $G^S(x', x_1)$  and  $G^S(x_2, x)$ , respectively, while the



**Figure 6.** An example of a set of component scattered waves that create non-physical, stationary energy within  $\mathcal{L}^A[G_{x',x_1}^S, G_{x',x}^S, G_{x_2,x}^S]$ . Key as Fig. 5.



**Figure 7.** One possible set of components that create a stationary contribution from  $\mathcal{L}^A[G_{x',x_1}^S, G_{x',x}^S, G_{x_2,x}^S]$  with the traveltime of a true multiply scattered event between source  $x_1$  and receiver  $x_2$ . Key as Fig. 5.

dashed line indicates the cross-correlated wave,  $G^S(x',x)$ . These figures therefore show that stationary phases can exhibit physical (Fig. 5) or non-physical (Fig. 6) traveltimes, depending on the geometry of the three constituent terms in  $\mathcal{L}^A[G_{x',x_1}^S, G_{x',x}^S, G_{x_2,x}^S]$ .

However, in principle, the construction of the traveltimes of all of the physical traveltimes in  $G^S(x_2, x_1)$  can still be attained whenever the three ray paths corresponding to  $G^S(x',x_1)$ ,  $G^S(x_2,x)$  and  $G^S(x',x)$  all mutually focus on an identical first (or last) scatterer. This is shown in Fig. 7, where one possible construction of the correct traveltime of an arbitrary multiply scattered event between source  $x_1$  and receiver  $x_2$  is displayed: cancellation of common paths [ $F$ -to- $x'$ ] and [ $x$ -to- $F$ ] leads to stationarity with respect to  $x$  and  $x'$ , and coincidence of the two singly scattered paths [ $x_1$ -to- $F$ -to- $x'$ ] and [ $x$ -to- $F$ -to- $x'$ ] and the multiply scattered path [ $x$ -to- $x_2$ ] at the scatterer  $F = 1$  ensures that the result of the interferometric operator  $\mathcal{L}^A[G_{x',x_1}^S, G_{x',x}^S, G_{x_2,x}^S]$  provides traveltime information of a physical scattering event between  $x_1$  and  $x_2$ . Since the three wavefields all focus on the same scatterer, the dynamic argument discussed for the single scattering problem (L er *et al.* 2014; Meles & Curtis 2013a) is still valid, and therefore  $\mathcal{L}^A[G_{x',x_1}^S, G_{x',x}^S, G_{x_2,x}^S]$  also represents a proxy for the true waveform of  $G^S(x_2, x_1)$ . This result holds irrespective of the specific scatterer on which the three wavefields  $G^S(x',x_1)$ ,  $G^S(x_2,x)$  and  $G^S(x',x)$  focus.

Events constructed by evaluating  $\mathcal{L}^A[G_{x',x_1}^S, G_{x',x}^S, G_{x_2,x}^S]$  can therefore be classified as physical or non-physical, provided that correct, mutually focused components can be identified and used in this operator to predict arrival times and moveouts of all physical, scattered waves. Any wave that is not thus predictable must be non-physical. In the next section, we will show how analysis of recorded data can provide the information invoked in Fig. 7 and thus reproduce any order of scattering kinematics through application of a prediction algorithm. We note again that the geometrical argument behind the method currently assumes point diffractors; its applicability to realistic scenarios will therefore depend on the extent to which this approximation is reasonable.

### PHYSICAL ENERGY PREDICTION IN WAVEFIELD INTERFEROMETRY

In this section, we illustrate the practical application of the prediction method. We compute wavefields with a numerical implementation of the 2-D Foldy method (Foldy 1945) from Galetti *et al.* (2013). This method is particularly useful for our purposes because it does not suffer from shortcomings usually associated with finite-difference modelling tools (i.e. numerical dispersion, spurious reflections from imperfectly absorbing boundaries, etc.) that can affect Green’s function estimates more severely than interferometry-related approximations (e.g. dipole to monopole approximation, Galetti *et al.* 2013). The Foldy method is also consistent with the acoustic optical theorem that determines the correct values of all scattering amplitudes such that energy is conserved for point scatterers problem (Groeneboom & Snieder 1995; Snieder *et al.* 2008).

We consider a background velocity of  $1000 \text{ m s}^{-1}$ , a unit density, and three isotropic point scatterers located below a line of 160 sources and 400 receivers (Fig. 8): for each source along the boundary, noise-free data are recorded at all of the receivers. Calculations are performed in the frequency domain, but for ease of interpretation, we present results in the time domain. A Ricker wavelet with central frequency of 30 Hz is used to generate all wavefields. The data from the line of sources and receivers are organized into a data cube, with each cube slice corresponding to a so-called common-source or a common-receiver gather (see Fig. 9). A gather (in the terminology of exploration seismology) is a collection or a subset of a data set; a common-source gather is simply the subset of data recorded at all receivers for single, fixed source, and vice versa for a common-receiver gather.

Since three different moveouts are identifiable (in this case by visual inspection) on each of these gathers (labelled 1, 2 and 3 in Figs 10a–c), and each moveout constitutes the fingerprint of an individual diffractor, we conclude that three scatterers are present in the model.

Any multiply scattered event is characterized by a scattering path, and each scattering path can be classified by a ‘first’ scatterer. Without any loss of generality, we therefore focus on all of the scattered events corresponding to any arbitrary first scatterer  $F$ . We will use the data from the synthetic experiment in Fig. 8 to illustrate.

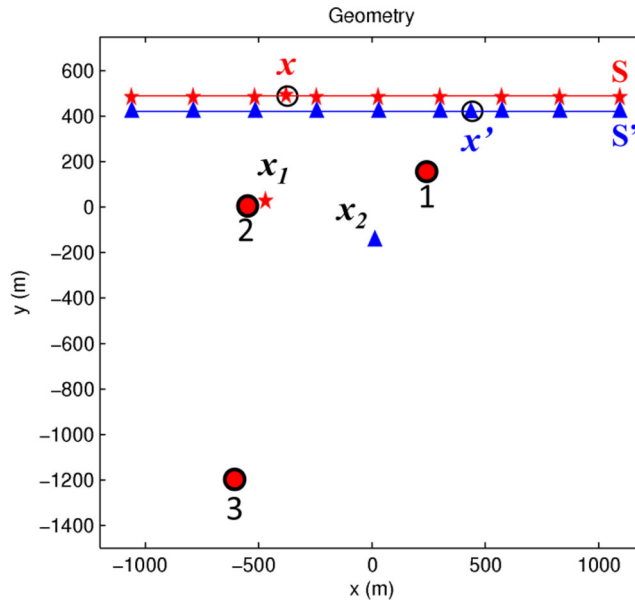


**Figure 8.** Geometry of the model used in numerical examples. Stars and triangles represent sources and receivers, respectively. Solid dots represent scatterers. A total of 160 sources and 400 receivers are employed in horizontal arrays (only every 20th source and 5th receiver is plotted for clarity). The 50th source and the 240th receiver (used in Fig. 10) are highlighted by circles.

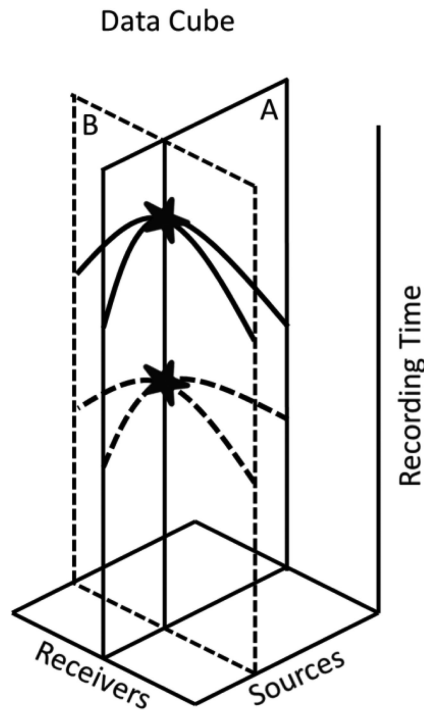


**Figure 9.** Schematic representation of a source and receiver gather data cube where recorded time series are organized to be vertical in recording time. A slice corresponding to a fixed receiver, A in the figure, is a common-receiver gather, while a slice at a specific source, B in the figure, is a common-source gather. At the intersection of these slices, all arriving energy must coincide (stars in the cartoon) because the recorded trace corresponds to the same source–receiver pair in both slices. Due to this continuity property, it is possible to identify source/receiver moveouts corresponding to the same arriving waves (solid and dashed curves).

To identify energy from the three events depicted in Fig. 7 from the data cube, we proceed as follows:

1. For an arbitrary boundary source–receiver pair  $(x', x)$ —here, we use  $(50, 240)$  as indicated in Fig. 8—consider the primary event associated with an arbitrary scatterer  $F$ . This is the component of  $G^S(x', x)$  that contributes to the construction of the multiply scattered event depicted in Fig. 7 (dashed line). Primaries are the observed scattered events with the shortest traveltimes for any given common-source or common-receiver moveout. Since arrivals on common-source and common-receiver gathers always converge at one point (Figs 9 and 10), by comparing

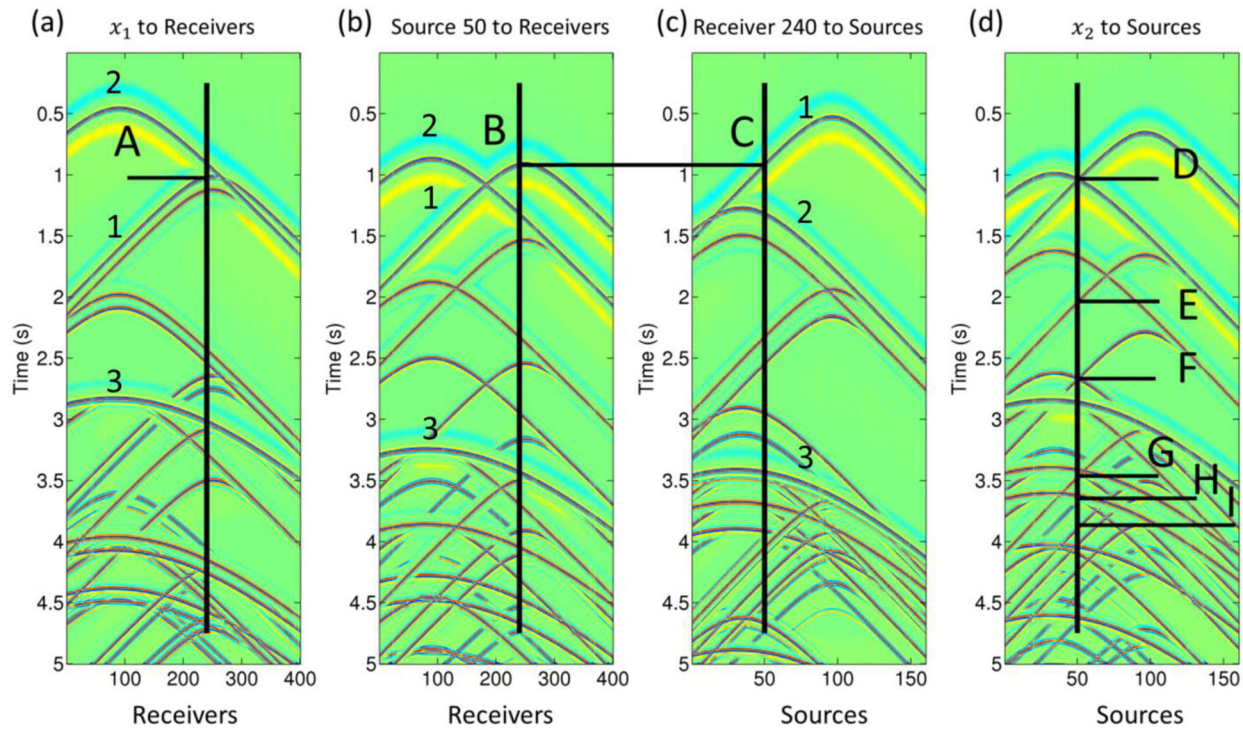


**Figure 10.** (a) Common-source gather for the source at  $x_1$ ; the black vertical line indicates the 240th receiver  $x'$  of Fig. 8. (b) Common-source gather for the 50th source  $x$  in Fig. 8; the black vertical line identifies the 240th receiver  $x'$  of Fig. 8 and panel (a). (c) Common-receiver gather for receiver 240; the vertical black line identifies the source 50 used in panel (b). (d) Common-receiver gather corresponding to the receiver at  $x_2$ . The direct wave has been removed from all of the gathers and a gain has been applied to the traces at later times to foster readability. Letters indicate arrivals referred to in the text. Numbers 1, 2 and 3 indicate the primary fingerprint of respective scatterers in Fig. 8.

primaries at the same source–receiver pair on both gathers we link common-source and common-receiver moveouts for any scatterer (see Figs 10b and c). Thus, we determine the full source-side and receiver-side *fingerprint* of the scatterer. Scatterers are then labelled by these primary moveouts (numbers in Fig. 10)—which together constitute the unique fingerprint of any diffractor. It is important to note again that we do not need to locate a scatterer or know anything about its properties; we can nevertheless label each one uniquely in this way, provided that the fingerprint or moveout is sufficiently distinct from those of the other scatterers. In the following, we use  $\text{FP}(S, S', F)$  to refer to the fingerprint—common-source and common-receiver gathers' primary (single-scattering) moveouts across source surface  $S$  and receiver surface  $S'$ , respectively, corresponding to scatterer  $F$ .

2. Consider the primary arrival corresponding to the source–receiver pair  $(x', x_1)$  (Fig. 10a) and the same scatterer  $F$ . As explained above, this event can be identified as it has the same common-source moveout as  $\text{FP}(S, S', F)$ , and represents the component of  $G^S(x', x_1)$  that is invoked in Fig. 7 (thin solid line). By cross-correlating these two events, we end up with a non-physical function that does not depend kinematically on  $x'$  since the phase of the common path connecting the receiver at  $x'$  to the scatterer is cancelled out by cross-correlating the two traces.

3. In the panel corresponding to the source–receiver pair  $(x_2, x)$  (Fig. 10d), consider any of the many other events showing the same common-receiver moveout as  $\text{FP}(S, S', F)$ , (C in Fig. 10c and D to I in Fig. 10d). Any such event represents the component of  $G^S(x_2, x)$  that is invoked in Fig. 7 (thick solid path), and each corresponds to a different multiple-scattering path. In practice, the correct common-receiver moveout can easily be found in the common-receiver gather by comparing the common-source and common-receiver gathers where they converge to have identical events (compare Figs 10b and c, and see Fig. 9).

4. Apply the SRI operator  $\mathcal{L}^A[G_{x', x_1}^S, G_{x', x}^S, G_{x_2, x}^S]$  for the three components identified above (here, requiring only that any of the arrivals found in step 3 is convolved with the non-physical results of step 2): as seen in Fig. 7, the result of this operation should have the exact traveltimes of a scattered event observed in  $G^S(x_2, x_1)$ . Moreover, since the three involved wavefields all focus on the same scatterer,  $\mathcal{L}^A[G_{x', x_1}^S, G_{x', x}^S, G_{x_2, x}^S]$  represents a proxy for  $G^S(x_2, x_1)$  (Lörer *et al.* 2014; Meles & Curtis 2013a).

Repetition of this procedure over all of the primary scatterers (there are as many as there are unique fingerprints in step 1), and over all multiply scattered paths (step 3) ultimately leads to the identification of all physical scattered events in the desired source–receiver Green's function. Any remaining unidentified energy in a Green's function reconstructed using the interferometry equations above when using only partial boundaries  $S$  and  $S'$ , therefore corresponds to non-physical or spurious energy.

If we only require traveltimes of physical waves to be predicted, note that it is not necessary to carry out the full correlations and convolutions involved in  $\mathcal{L}^A[G_{x', x_1}^S, G_{x', x}^S, G_{x_2, x}^S]$ . Since cross-correlation subtracts phases and hence traveltimes of the correlated waves, whereas convolution adds them, it is only necessary to pick the arrival times of each of the above waves and subtract or add them as specified

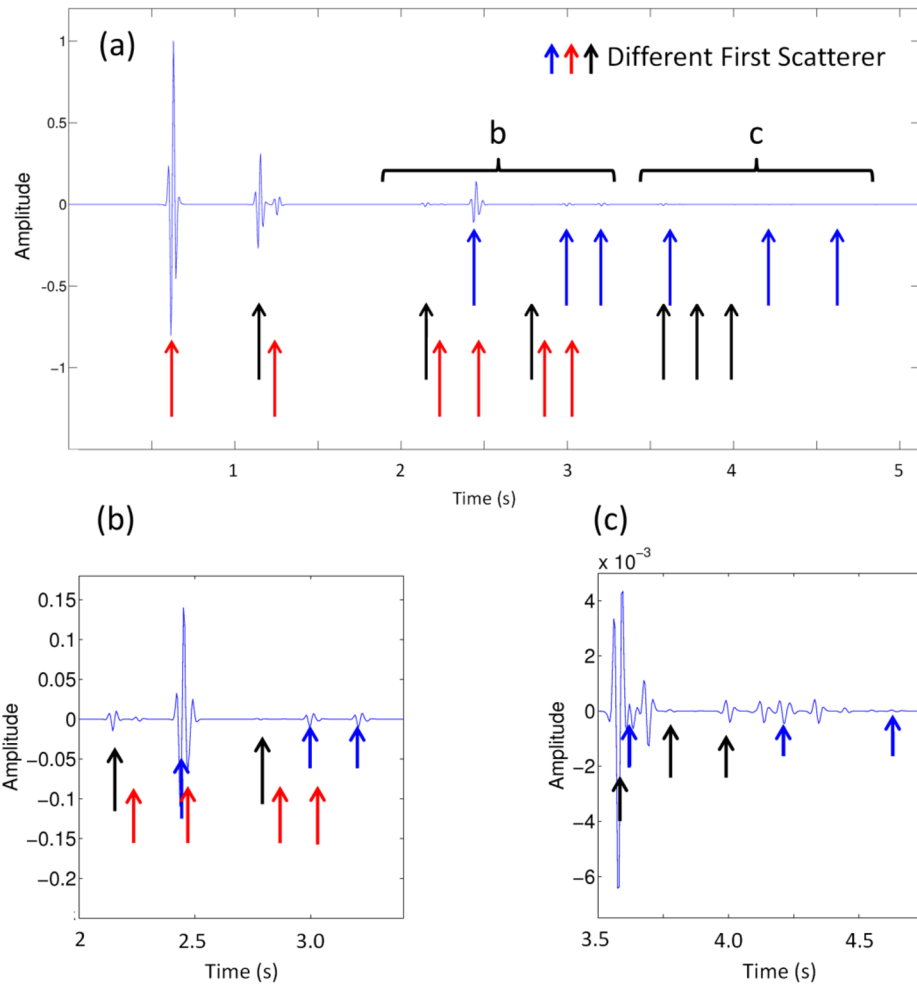


**Figure 11.** For the geometry displayed in Fig. 8 and algorithm depicted in Fig. 7 and described in the text, this figure shows the correct (directly modelled) scattered Green's Function between  $x_1$  and  $x_2$  and the expected traveltimes corresponding to (possibly multiply) scattered events associated with each of the three different first scatterers (different colours). Labels b and c are magnified in (b) and (c) with different vertical axis scales to enhance visibility of arrivals.

in  $\mathcal{L}^A[G_{x',x_1}^S, G_{x',x}^S, G_{x_2,x}^S]$ . The result will be the traveltimes of the physical scattered waves. This is illustrated in the example below, and in Fig. 11.

### EXAMPLE: THREE POINT SCATTERERS

For the geometry depicted in Fig. 8 and the data displayed in Fig. 10, we present here results of the prediction algorithm and actual waveform interferometric reconstructions. First, we manually picked traveltimes of each of the required waveform arrivals used in  $\mathcal{L}^A[G_{x',x_1}^S, G_{x',x}^S, G_{x_2,x}^S]$  using panels in Fig. 10. We then added or subtracted these traveltimes as prescribed by correlations or convolutions in  $\mathcal{L}^A[G_{x',x_1}^S, G_{x',x}^S, G_{x_2,x}^S]$ . Fig. 11(a) shows the superposition of the exact, directly modelled scattered wave  $G^S(x_2, x_1)$  and the corresponding predicted traveltimes. The match is rather good and is not limited to first-order scattering events: in Fig. 11(b), late portions of the waveform, involving multiple-scattering events of extremely low amplitude, are presented. Only a few events are not matched due to the increasing complexity of the seismograms in Fig. 10 and the corresponding difficulty in moveout identification at longer observation times. Traveltimes prediction is a particularly important and intrinsic property of the method, which for media that only contain diffractors in otherwise smoothly varying fields is totally data-driven. It also does not introduce any cumulative error, in the sense that mis-identification or mis-picking of a single scattering event in Fig. 10(d) does not affect the results for others (provided that primaries are correctly picked in Figs 10a–c).

Waveforms constructed by evaluating  $\mathcal{L}^A[G_{x',x_1}^S, G_{x',x}^S, G_{x_2,x}^S]$  for the complete scattered waveform recorded in the configuration of Fig. 8 are displayed in Figs 12 and 13. Considering that only one of seven terms in eq. (11) is used, the reconstruction of the scattered wavefields is good, and apart from relative amplitude errors in different arrivals, only relatively minor non-physical artefacts contaminate the estimated Green's function. These artefacts are due to the indiscriminate application of  $\mathcal{L}^A[G_{x',x_1}^S, G_{x',x}^S, G_{x_2,x}^S]$  to the whole scattered waveform rather than to only the few events picked manually during the above traveltimes prediction algorithm. However, since the traveltimes of true scattered waves can be evaluated by means of the traveltimes prediction algorithm, these artefacts can now be identified and ignored. In the early and

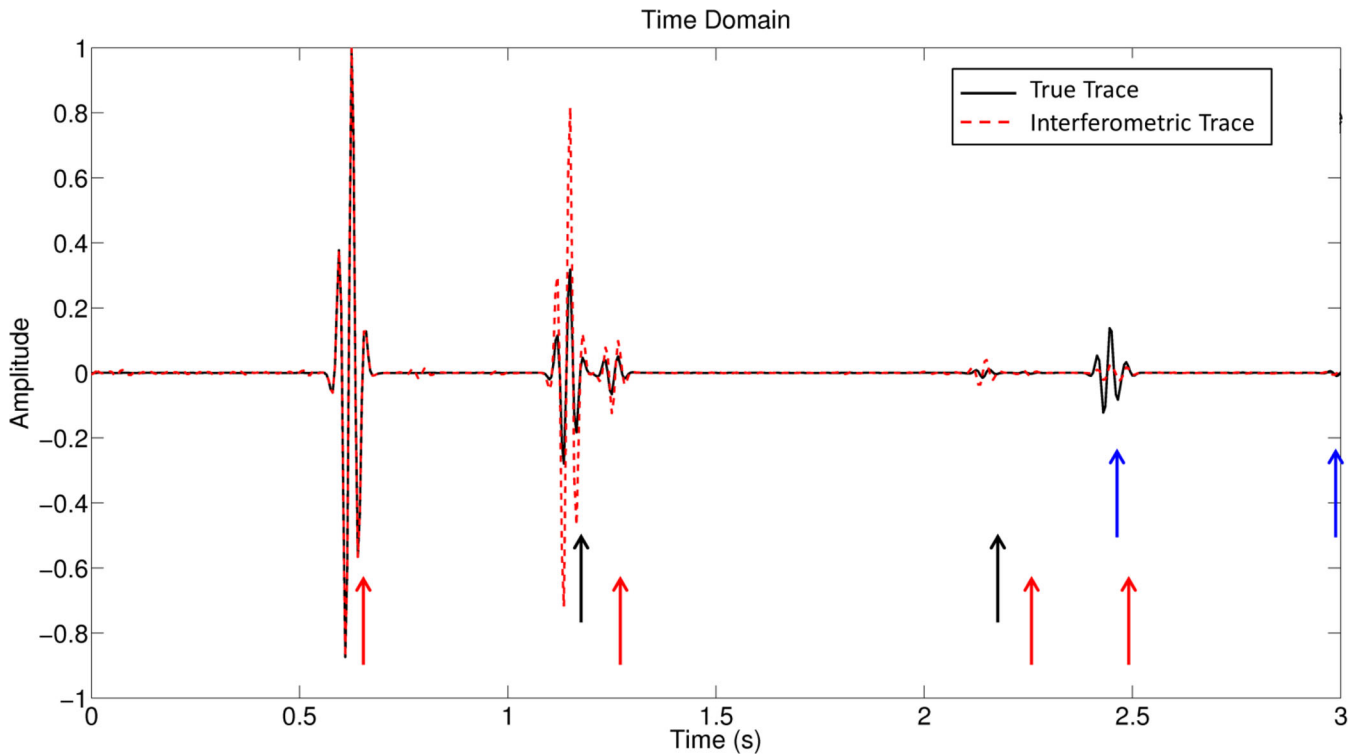


**Figure 12.** For the geometry displayed in Fig. 8, the actual scattered field (solid curve) and the field reconstructed by SRI using only  $\mathcal{L}^A[G_{x',x_1}^S, G_{x',x}^S, G_{x_2,x}^S]$  (dashed curve). Both traces are normalized by their maximum amplitude. Application of the procedure discussed in the text allows non-physical events (like the tiny arrival around 0.8—see also Fig. 13) to be identified and ignored.

most often relevant part of the waveform (Figs 12 and 13a), the one-to-one correspondence between expected and observed signals is robust, and it is only in the later portion that the traveltimes prediction algorithm fails (Fig. 13b). In this part of the signal, artefacts are particularly problematic because they exhibit traveltimes close to those of physical energy and are therefore difficult to interpret as non-physical (see Fig. 13b). However, an automated picking algorithm could be used to suppress artefacts by selectively evaluating  $\mathcal{L}^A[G_{x',x_1}^S, G_{x',x}^S, G_{x_2,x}^S]$  only on the appropriate scattered events.

Manipulation of the data used in the traveltimes prediction algorithm can predict *any* scattered signal. However, there are additional stationary combinations of scattered data components that would equally provide physical energy, despite not focusing on the first or a single identical scatterer (as required in the presented algorithm). This is illustrated in Fig. 14 and discussed later for Fig. 18. Because the configuration in Fig. 14 involves higher order scattering events than those presented in Figs 7 and 18, their amplitudes are usually negligible and hence are ignored in this paper.

The benefit of discriminating physical from non-physical energy becomes more appreciable in the second set of synthetic experimental results shown in Fig. 15. In this case, a much coarser sampling of sources and receivers was used: only 40 out of 160 sources, and 40 out of 400 receivers spanned the same horizontal interval as in Fig. 8. Due to the depleted coverage, the reconstruction provided by the evaluation of  $\mathcal{L}^A[G_{x',x_1}^S, G_{x',x}^S, G_{x_2,x}^S]$  is deteriorated by the introduction of many spurious events (Fig. 15a). However, the identification algorithm can still be applied in this case and discriminates between physical and non-physical events, since moveout identification is still possible (Fig. 15b).

A third example illustrates the potential of the proposed method. In this case, the source and receiver spatial sampling interval on  $S$  and  $S'$  was the same as in Fig. 8 (see Fig. 16a) but again only 40 sources and 40 receivers were used so that the lateral extent of  $S$  and  $S'$  was far more limited. Instead of being contaminated by diffuse clutter as in Fig. 15(a), in this case, the reconstruction provided by the evaluation of  $\mathcal{L}^A[G_{x',x_1}^S, G_{x',x}^S, G_{x_2,x}^S]$  suffers from high-resolution artefacts both at negative and positive times (Fig. 16b). However, it is still possible to identify the three different common-source and common-receiver moveouts (see Fig. 16c, which shows the limited gather portions that are available in this geometry), and therefore to apply the above algorithm. We can thus reject as spurious the erroneously reconstructed energy.

For the geometry depicted in Fig. 8, Fig. 17(a) shows the results obtained by applying the sum of the seven operators that constitutes the left-hand side of eq. (11), and also  $\mathcal{L}^A[G_{x',x_1}^S, G_{x',x}^S, G_{x_2,x}^S]$  alone, to the available data (solid dotted and dashed traces, respectively) as compared to the true scattered wavefield (solid line). The poor fit of the solid dotted curve to the solid curve clearly indicates that the result of applying all of eq. (11) is strongly affected by the incompleteness of the boundary, while  $\mathcal{L}^A[G_{x',x_1}^S, G_{x',x}^S, G_{x_2,x}^S]$  is relatively robust to that incompleteness (compare dashed and solid curves). This apparently paradoxical result holds for two reasons. First, stationarity is associated with physical and non-physical energy for terms that involve direct waves (Löer *et al.* 2014). Purely scattered waves produce only physical energy in  $\mathcal{L}^A[G_{x',x_1}^S, G_{x',x}^S, G_{x_2,x}^S]$ , at least for the single scattering problem (Meles & Curtis 2013a), while the non-physical

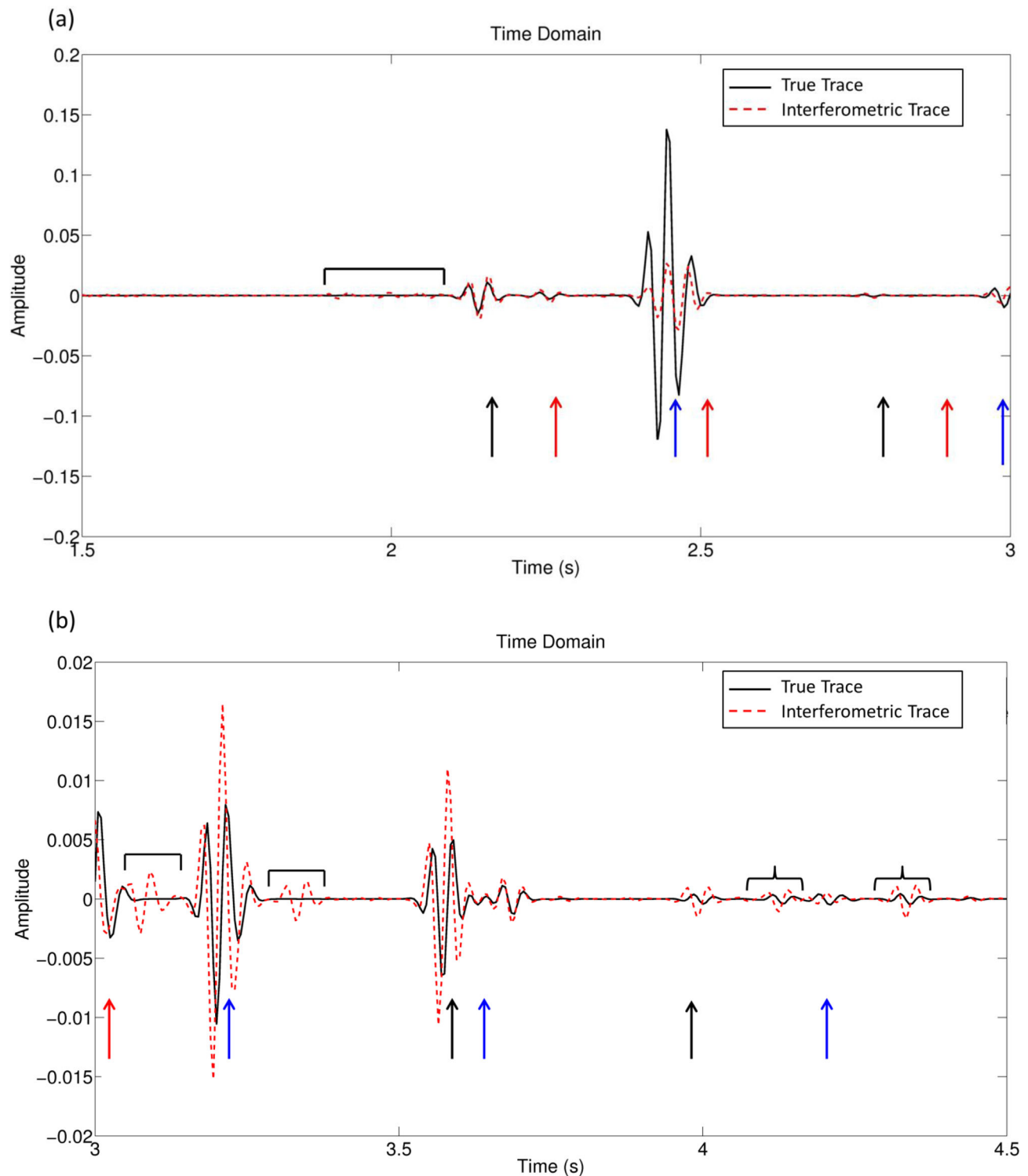


**Figure 13.** As for Fig. 12, but only a portion of the wavefield is displayed, amplified for ease of comparison. The arrows are the same as in Fig. 11. Square brackets indicate non-physical energy that was (correctly) not predicted by the algorithm. Curly brackets indicate physical energy that should have been but was not identified by the algorithm. In the early and most often relevant part of the waveform (Figs 12 and 13a), the one-to-one correspondence between expected and observed signals is robust, and it is only in the later portion that the traveltime prediction algorithm fails (Fig. 13b). The relatively poor performance of the method at later times is due to the corresponding complexity in the seismograms (see Fig. 10). The erroneous reconstruction of some of the later events in (b) is only due to contamination of stationary non-physical events occurring at times comparable to those of the physical events (see Fig. 6), and to edge effects from the truncated source and receiver arrays used in the evaluation of  $\mathcal{L}^A[G_{x',x_1}^S, G_{x',x}^S, G_{x_2,x}^S]$ . The traveltime prediction algorithm thus proves to be more stable than the waveform reconstruction obtained through evaluation of  $\mathcal{L}^A[G_{x',x_1}^S, G_{x',x}^S, G_{x_2,x}^S]$ .

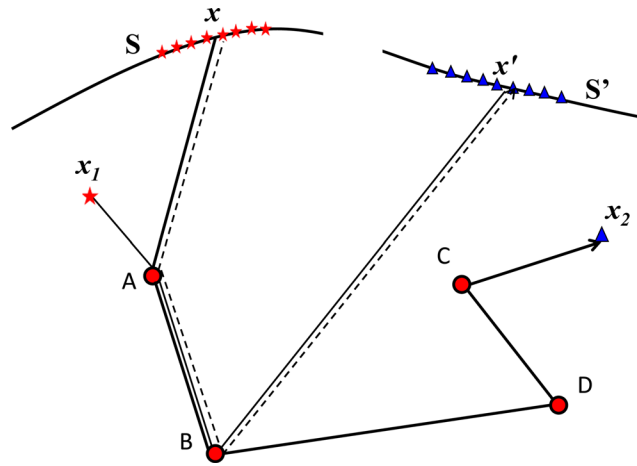


**Figure 14.** A geometry for which cancellation of traveltimes along repeated solid and dashed ray paths results in the correct traveltime from  $x_1$  to  $x_2$ . Thus, combinations of scattered components resulting in stationary and physical energy associated with  $G^S(x_2, x_1)$  are not limited to those used in the deduction of the traveltime prediction algorithm above (where only primaries between  $x$  and  $x'$  were considered). However, higher order scattering events are used in the above construction, and the corresponding contributions to physical energy are negligible.

terms associated with  $\mathcal{L}^A[G_{x',x_1}^S, G_{x',x}^S, G_{x_2,x}^S]$  when multiple scatterers are present are of relatively low amplitude. Second, coarse gridding of sources and receivers breaks down the validity of the stationary phase approach, which is based on mutual cancellation or summation of slightly out-of-phase (at non-stationary points) or in-phase (at stationary points) wavefields, respectively. This is critical for the first six terms of the right-hand side of eq. (11), because any point may constructively contribute to the final result of the integral if cancellation of its contribution by neighbouring points does not take place because the neighbour is missing. Such fragmentation of the integrals is not critical for the stationary point pairs associated with  $\mathcal{L}^A[G_{x',x_1}^S, G_{x',x}^S, G_{x_2,x}^S]$ , since all parts of the integral are stationary and hence provide the same physical kinematic contribution.

The instability with respect to gridding density of various terms of the right-hand side of eq. (11) is evident in Fig. 17(b) which corresponds to the coarser geometry discussed in Fig. 15. The worsening of the fit between the solid dotted and the solid curves indicates the critical instability of eq. (11) with respect to spatial sampling density. As expected, the coarser sampling is not as detrimental to the performance of  $\mathcal{L}^A[G_{x',x_1}^S, G_{x',x}^S, G_{x_2,x}^S]$  (the fit between the dashed and the solid curve is still reasonably good).

## DISCUSSION

We have presented a method to identify traveltimes of multiply scattered physical energy in SRI based on moveout analysis. This allows the discrimination of physical and non-physical energy in estimated Green's function. We have seen that coincidence at common scatterers of the three ray paths involved in the SRI trilinear, purely scattered-wave operator can provide a good approximation to physical energy (Fig. 7), and have devised an algorithm to identify the energy involved in common-source and common-receiver gathers based on fingerprinting of the first scatterer in the scattering path. Iterating the method over all possible first scatterers allows the identification of any physical multiply scattered event, and the classification of all scattered wave energy by the first scatterer involved.

Alternative methods, which focus on the last, or on intermediate scatterers, are also possible using geometries depicted in Figs 18(a) and (b). Again, in Fig. 18(a), cancellation of common paths  $[L\text{-to-}x']$  and  $[x\text{-to-}L]$  leads to stationarity, but only coincidence of the two singly scattered paths  $[x\text{-to-}L\text{-to-}x_2]$  and  $[x\text{-to-}L\text{-to-}x']$  and the multiply scattered path  $[x_1\text{-to-}x']$  at the scatterer  $L$  ensures that the result of the interferometric operator  $\mathcal{L}^A[G_{x',x_1}^S, G_{x',x}^S, G_{x_2,x}^S]$  provides information of a physically scattered event between  $x_1$  and  $x_2$ . Similarly in Fig. 18(b), cancellation of common paths  $[G\text{-to-}x']$  and  $[x\text{-to-}G]$  leads to stationarity, but only coincidence of the singly scattered path  $[x\text{-to-}G\text{-to-}x']$  and the multiply scattered paths  $[x_1\text{-to-}G\text{-to-}x']$  and  $[x\text{-to-}G\text{-to-}x_2]$  at the scatterer  $G$  ensures that the result of the interferometric operator  $\mathcal{L}^A[G_{x',x_1}^S, G_{x',x}^S, G_{x_2,x}^S]$  provides information of a physically scattered event between  $x_1$  and  $x_2$ . However, in contrast to the configuration depicted in Figs 7 and 18(a), only one of the three ray paths involves a first-order scattering event, thus complicating the applicability of the identification algorithm. In addition, this latter geometry would only recover multiple-scattering events (the path  $[x_1\text{-to-}G]$  being common to all reconstructed arrivals). Nevertheless, the fact that all of these various contributions provide proxies for physical energy to the interferometric result may contribute to the apparent stability of SRI waveform estimates using  $\mathcal{L}^A[G_{x',x_1}^S, G_{x',x}^S, G_{x_2,x}^S]$  as observed above.

Diffracted waves can be used profitably in imaging as theoretically they provide high-resolution information about sharp boundaries, faults, scatterers, etc. In addition, discrimination, identification and analysis of singly and multiply scattered waves can help in enhancing desired signals or suppressing clutter in seismograms.

Meles & Curtis (2013a) have shown that SRI is particularly suitable to reconstruct scattered waveform information in single diffractor problems. Here, we have extended this theory to multiple scatterers, showing that despite the increased complexity, good quality reconstructions based on purely scattered waves confirmed the validity of the evaluation of  $\mathcal{L}^A[G_{x',x_1}^S, G_{x',x}^S, G_{x_2,x}^S]$  as a proxy for physically scattered waves.

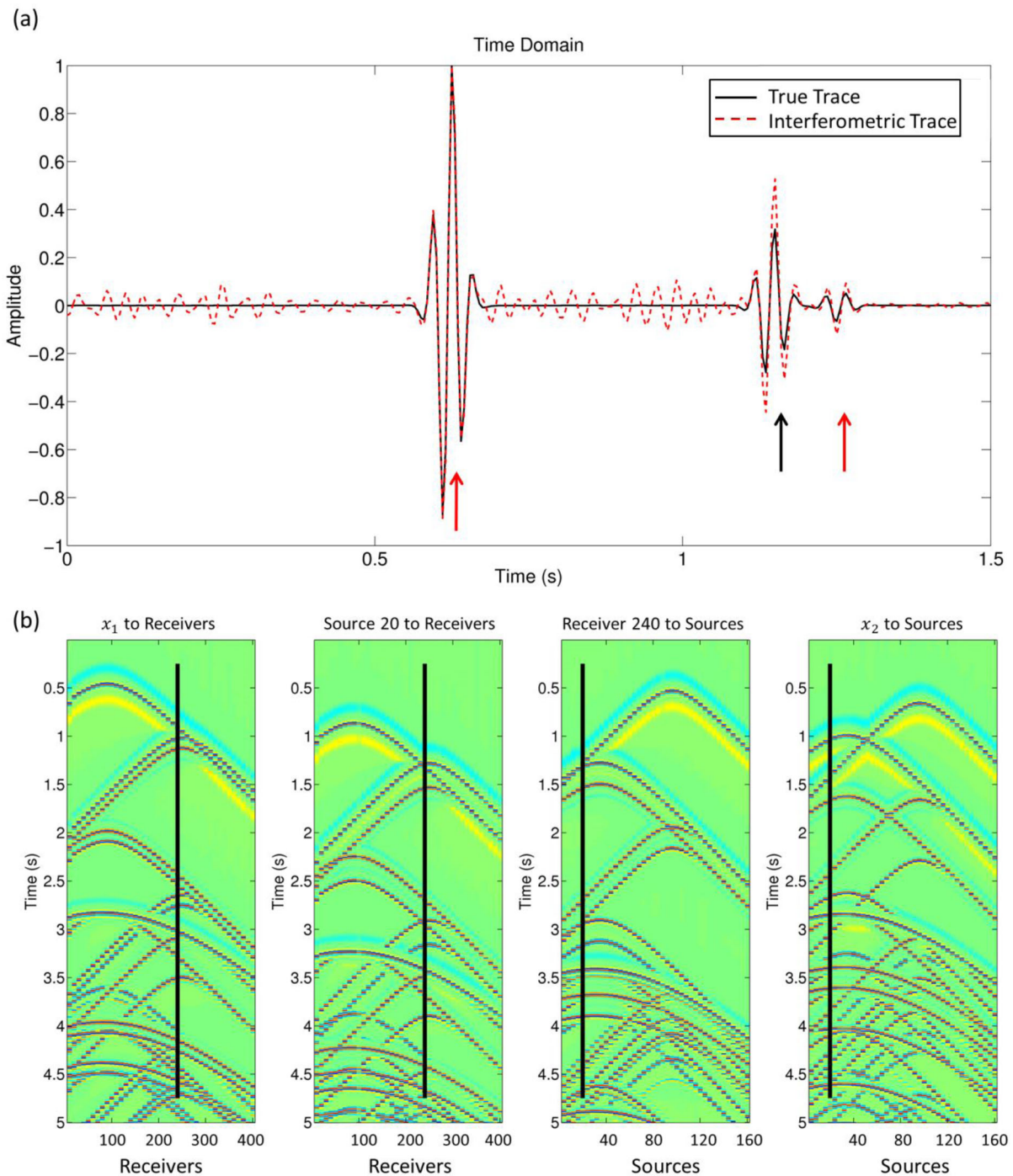


**Figure 15.** Results from the second experiment. (a) Green's function estimate resulting from evaluation of  $\mathcal{L}^A[G_{x'_1, x_1}^S, G_{x'_1, x}^S, G_{x_2, x}^S]$  using only 40 sources and 40 receivers spanning the same surface extent as in Fig. 8, but with considerably coarser spatial sampling. Large-amplitude artefacts contaminate the entire signal. However, identification of the three common-source and common-receiver moveouts, and therefore prediction of traveltimes of the physical energy [arrows in part (a)] is still possible despite the lower coverage (compare Figs 15b and 10).

In contrast with standard interreceiver interferometry (Snieder & Fleury 2010), access to particular model- and configuration-dependent stationary points associated with other kind of interferometry is not required. As for the single scattering problems, this holds true because the operations prescribed by SRI result in the transformation of intermediate, non-physical waves into proxies of physical waves. In fact, these can be shown to be non-physical waves that exactly emulate physical waves (Löer *et al.* 2014), but the results presented here are unaffected by this.

While other methods can predict free surface-related, multiply diffracted waves (Verschuur *et al.* 2007), to our knowledge, this is the first data-driven algorithm for traveltime prediction of *internal* (subsurface) multiply diffracted waves simply by wavefield analysis. More specifically, our method does not require any additional wavefield or model estimation, as opposed to more complex and general algorithms

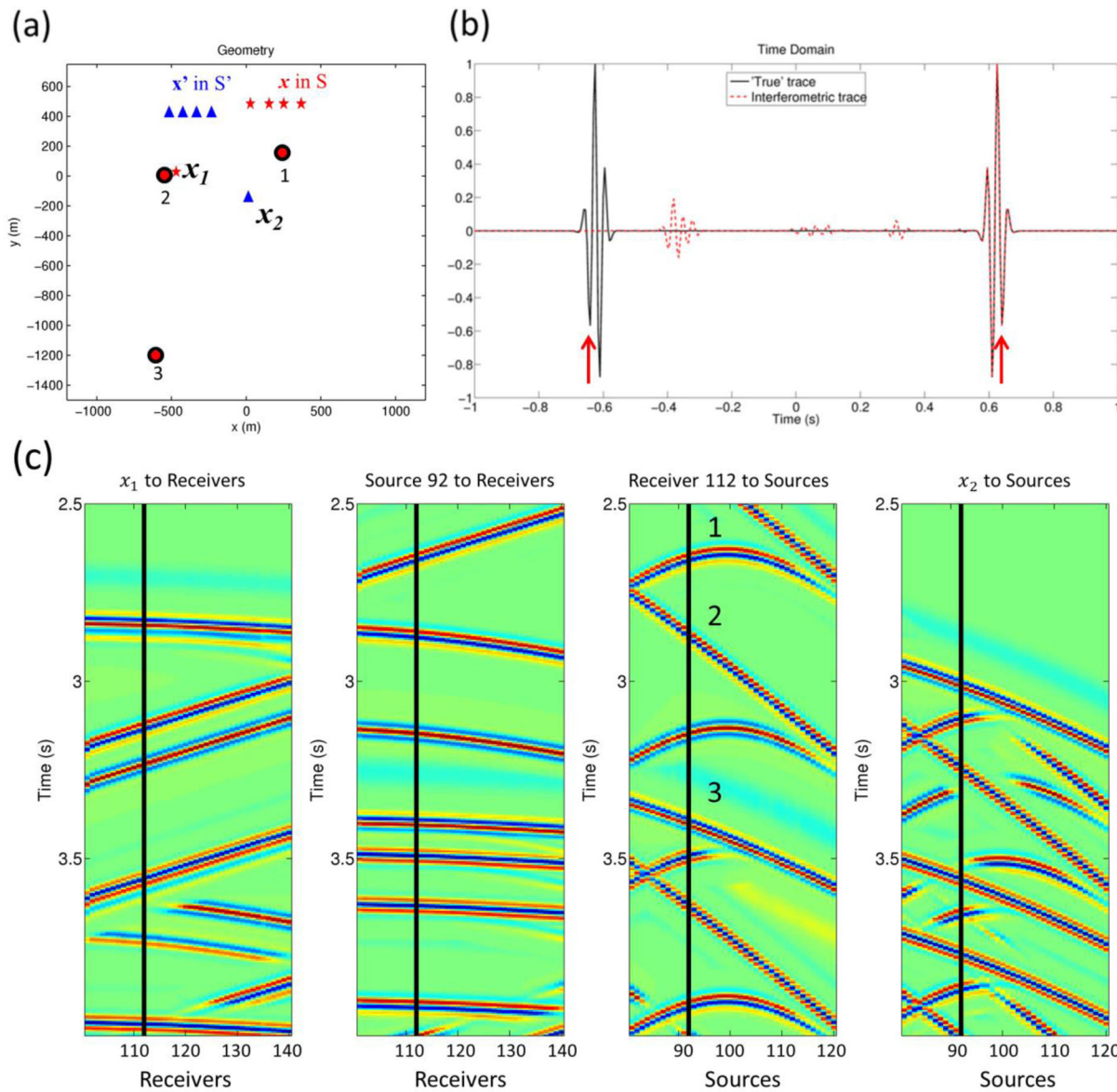


**Figure 16.** (a) Geometry of the third experiment. The same figure key and scatterer geometry as in Fig. 8 is used, but only 40 sources and 40 receivers are employed in the geometry shown here. (b) Green’s function estimate resulting from the evaluation of  $\mathcal{L}^A[G_{x',x_1}^S, G_{x',x'}^S, G_{x_2,x}^S]$ ; large-amplitude, localized artefacts contaminate the trace. (c) Identification of the three common-source and common-receiver moveouts, and therefore calculation of traveltimes of physical energy [arrows in part (b)] is still possible despite the lower coverage (compare Figs 16c and 10).

(Weglein *et al.* 1997; Wapenaar *et al.* 2013). Extension of the method to more general problems that also involve reflections will be the topic of future research. While designed and theoretically supported in the context of SRI, the method proposed here can also be understood simply on the basis of a kinematic analysis. However, when applied to interferometrically estimated scattered wavefields, it is clearly associated with interferometric representation theorems (eqs 10 and 11).

The algorithm has proved to be stable with respect to both boundary source and receiver coverage and sampling, thus potentially providing a flexible tool for practical application. An implication of this work is that if source or receiver coverage on the boundaries is limited, it may be better to use only the term  $\mathcal{L}^A[G_{x',x_1}^S, G_{x',x}^S, G_{x_2,x}^S]$  for reconstructions, rather than the full expression in eqs (10) and (11). Other terms on the right-hand side of these equations do not share the same stability with respect to coverage and sampling.

**ACKNOWLEDGEMENTS**

The authors thank the Edinburgh Interferometry Project (EIP) sponsors (ConocoPhillips, Schlumberger, Statoil and Total) for supporting this research. We are grateful to Ivan Vasconcelos (Schlumberger Gould Research, UK) for insightful discussions.

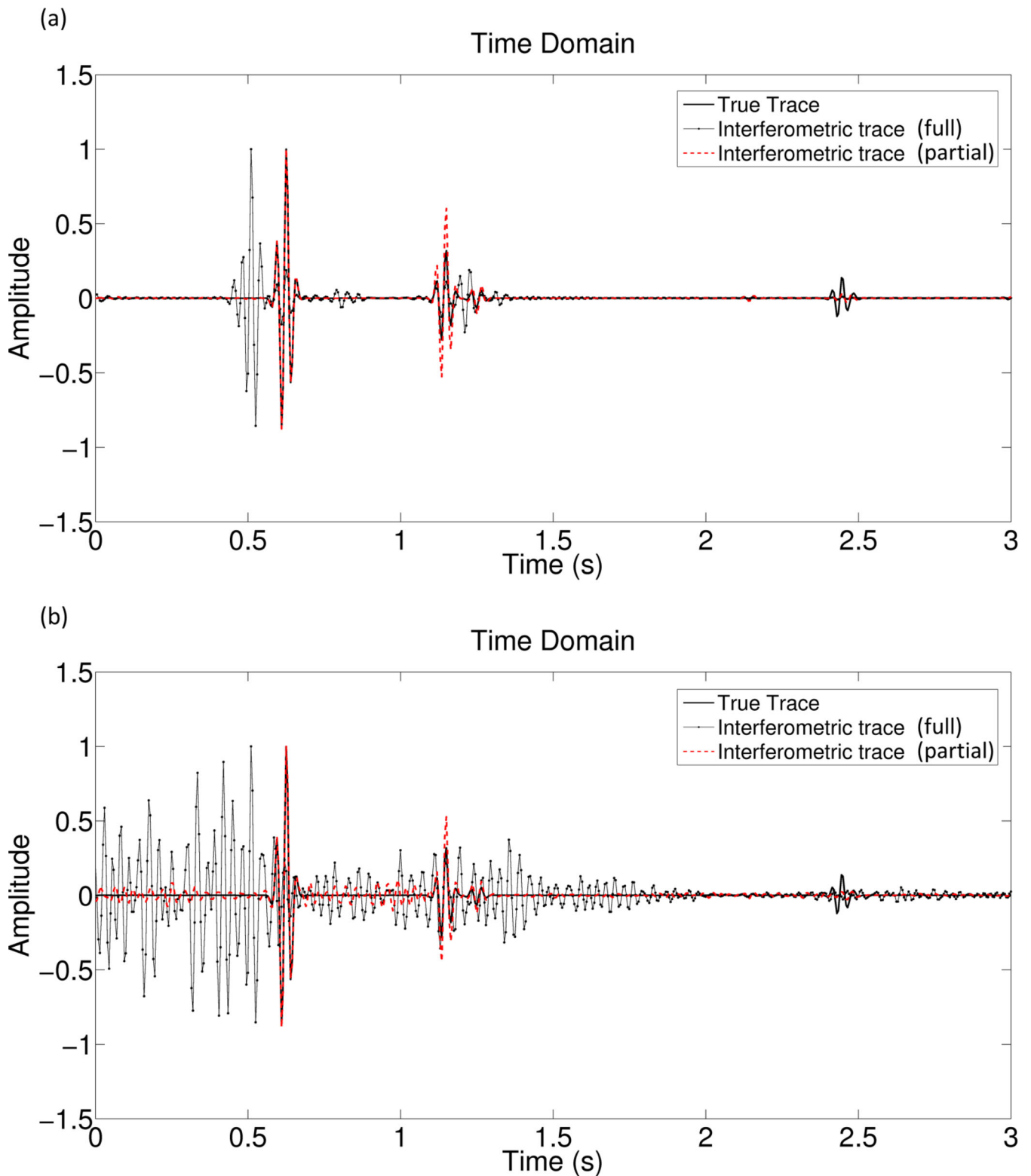


**Figure 17.** (a) For the geometry depicted in Fig. 8, comparison of true scattered trace (solid) and interferometric reconstructions provided by the full equation (11) (solid dotted curve) and by evaluation of  $\mathcal{L}^A[G_{x',x_1}^S, G_{x',x}^S, G_{x_2,x}^S]$  only (dashed curve). Artefacts contaminating the solid dotted curve are mainly associated with stationary non-physical point pairs. (b) As for (a), but for the coarser coverage employed for the example of Fig. 15. Most of the artefacts contaminating the solid dotted curve are now due to non-stationary point contributions not being cancelled out by slightly out of phase neighbouring wavefield recordings. The stationary *planes* associated with  $\mathcal{L}^A[G_{x',x_1}^S, G_{x',x}^S, G_{x_2,x}^S]$  (dashed curve) are clearly less sensitive to coarser coverage than are the other components of the right-hand side of eq. (11), and hence have fewer contaminating artefacts. All traces are normalized to their maximum amplitude.

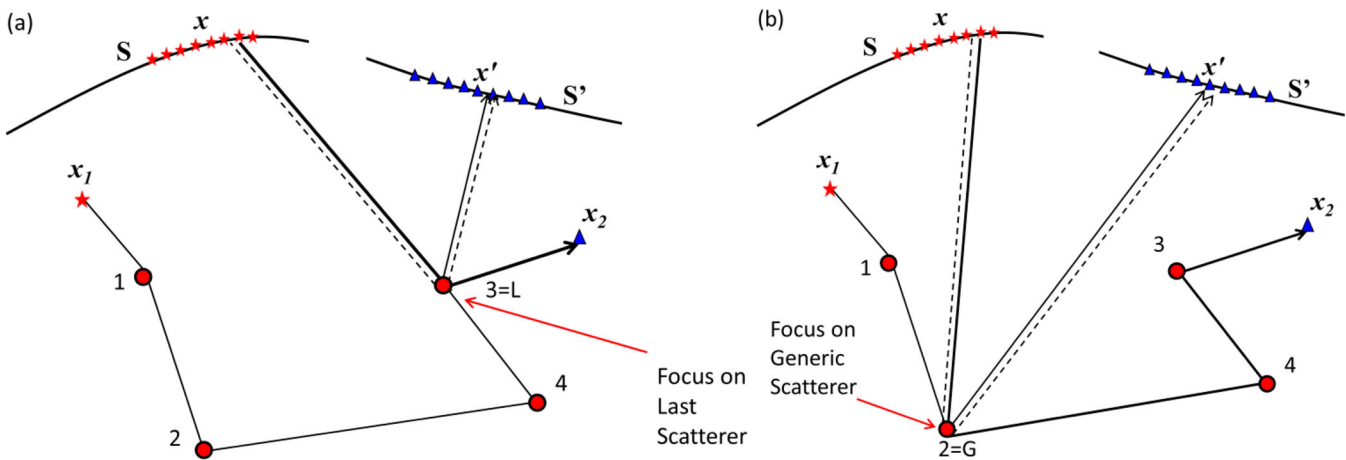


**Figure 18.** Other possible configurations that allow the construction of the correct traveltime of a multiply scattered wave between source  $x_1$  and receiver  $x_2$ .

## REFERENCES

- Bharadwaj, P., Schuster, G., Mallinson, I. & Dai, W., 2011. Theory of supervirtual refraction interferometry, *Geophys. J. Int.*, **178**, 419–446.
- Campillo, M. & Paul, A., 2003. Long range correlations in the seismic coda. *Science*, **299**, 547–549.
- Claerbout, J.F., 1968. Synthesis of a layered medium from its acoustic transmission response, *Geophysics*, **33**, 264–269.
- Curtis, A., 2009. Source-receiver seismic interferometry, in *Proceedings of Society of Exploration Geophysics, Annual Meeting Extended Abstracts*, pp. 3655–3658.
- Curtis, A. & Halliday, D., 2010. Source-receiver wave field interferometry, *Phys. Rev. E*, **81**, 046601-1–046601-10.
- Curtis, A., Behr, Y., Entwistle, E., Galetti, E., Townend, J. & Bannister, S., 2012. The benefit of hindsight in observational science: retrospective seismological observations, *Earth planet. Sci. Lett.*, **345–348**, 212–220.
- Curtis, A., Nicolson, H., Halliday, D., Trampert, J. & Baptie, B., 2009. Virtual seismometers in the subsurface of the Earth from seismic interferometry, *Nature Geosci.*, **2**, 700–704.
- Duguid, C., Halliday, D. & Curtis, A., 2011. Source-receiver interferometry for seismic wavefield construction and ground removal, *Leading Edge*, **30**, 838–843.
- Foldy, L.L., 1945. The multiple scattering of waves. I. General theory of isotropic scattering by randomly distributed scatterers, *Phys. Rev.*, **67**, 107–119.
- Galetti, E., Halliday, D. & Curtis, A., 2013. A simple and exact acoustic wavefield modelling code for data processing, imaging and interferometry applications, *Geophysics*, **78**, F17–F27.
- Grasmueck, M., Moser, T.J. & Pellisier, M.A., 2012. Stop treating diffractions as noise – use them for imaging of fractures and Karts, in *Proceedings of Hedberg Research Conference, Expanded Abstract*.
- Groeneboom, J. & Snieder, R., 1995. Attenuation, dispersion, and anisotropy by multiple scattering of transmitted waves through distributions of scatterers, *J. acoust. Soc. Am.*, **98**, 3482–3492.
- Hagedoorn, J.G., 1954. A process of seismic reflection interpretation, *Geophys. Prospect.*, **2**, 85–127.
- Halliday, D. & Curtis, A., 2010. An interferometric theory of source-receiver scattering and imaging, *Geophysics*, **75**(6), SA95–SA103.
- Hong, T.K. & Menke, W., 2006. Tomographic investigation of the wear along the San Jacinto fault, southern California, *Phys. Earth planet. Inter.*, **155**, 236–248.
- Khaidukov, V., Landa, E. & Moser, T.J., 2004. Diffraction imaging by focusing-defocusing: an outlook on seismic superresolution, *Geophysics*, **69**(6), 1478–1490.
- King, S. & Curtis, A., 2012. Suppressing nonphysical reflections in Green's function estimates using source-receiver interferometry, *Geophysics*, **77**, Q15–Q25.
- Klem-Musatov, K., 1994. *Theory of Seismic Diffractions*, eds Hron, F. & Lines, L., SEG.
- Krey, T., 1952. The significance of diffraction in the investigation of faults, *Geophysics*, **17**, 843–858.
- Landa, E., Shtivelman, V. & Gelchinsky, B., 1987. A method for detection of diffracted waves on common-offset sections, *Geophys. Prospect.*, **35**, 359–374.
- Löer, K., Meles, G.A., Curtis, A. & Vasconcelos, I., 2014. Diffracted and pseudo-physical waves from spatially limited arrays using source-receiver interferometry (SRI), *Geophys. J. Int.*, **196**, 1043–1059.
- Meles, G.A. & Curtis, A., 2013a. Physical and non-physical energy in scattered wave source-receiver interferometry, *J. acoust. Soc. Am.*, **133**, 3790–3801.
- Meles, G.A. & Curtis, A., 2013b. Finger-printing diffractors encountered by multiply-scattered waves, in *Proceedings of 75th European Association of Geoscientists and Engineers Conference, Extended Abstract*.
- Neidell, N.S., 1997. Perceptions in seismic imaging, part 2: reflective and diffractive contributions to seismic imaging, *Leading Edge*, **16**, 1121–1123.
- Papziner, U. & Nick, K.P., 1998. Automatic detection of hyperbolas in georadargrams by slant-stack processing and migration, *First Break*, **16**, 219–223.
- Poliannikov, O.V., 2011. Retrieving reflections by source-receiver wavefield interferometry, *Geophysics*, **76**, SA1–SA8.
- Poliannikov, S.R. & Ling, C., 2012. Interferometric imaging of the underside of a subducting crust, *Geophys. J. Int.*, **189**(1), 681–690.
- Rickett, J. & Claerbout, J., 1999. Acoustic daylight imaging via spectral factorization: helioseismology and reservoir monitoring, *Leading Edge*, **18**, 957–960.
- Snieder, R. & Fleury, C., 2010. Cancellation of spurious arrivals in Green's function retrieval of multiple scattered waves, *J. acoust. Soc. Am.*, **128**, 1598–1605.
- Snieder, R., van Wijk, K., Haney, M. & Calvert, R., 2008. Cancellation of spurious arrivals in Green's function extraction and the generalized optical theorem, *Phys. Rev. E*, **78**, 036606, doi:10.1103/PhysRevE.78.036606.
- Snieder, R., Wapenaar, K. & Larner, K., 2006. Spurious multiples in seismic interferometry of primaries, *Geophysics*, **78**, S1111–S1124.
- van Manen, D.J., Robertsson, J.O.A. & Curtis, A., 2005. Modeling of wave propagation in inhomogeneous media, *Phys. Rev. Lett.*, **94**(16), 164301, doi:10.1103/PhysRevLett.94.164301.
- Vasconcelos, I., 2011. Source-receiver reverse-time imaging of vector-acoustic seismic data, in *81st Annual International Meeting, SEG Expanded Abstracts*, pp. 3184–3189.

- Vasconcelos, I., Snieder, R. & Douma, H., 2009. Representation theorems and Green's function retrieval for scattering in acoustic media, in *Proceedings of Society of Exploration Geophysics, Annual Meeting Extended Abstracts*, pp. 3184–3189.
- Verschuur, D. J., Wang, D. & Herrmann, F. J., 2007. Multiterm multiple prediction using separated reflections and diffractions combined with curvelet-based subtraction, in *SEG Technical Program Expanded Abstracts*, vol. 26, pp. 2535–2539
- Wapenaar, K., 2004. Retrieving the elastodynamic Green's function of an arbitrary inhomogeneous medium by cross correlation, *Phys. Rev. Lett.*, **93**, 254 301-1–254 301-4.
- Wapenaar, K. & Fokkema, J., 2006. Green's function representations for seismic interferometry, *Geophysics*, **71**(4), SI33–SI46.
- Wapenaar, K., Broggini, F., Slob, E. & Snieder, R., 2013. Three-dimensional single-sided Marchenko inverse scattering, data-driven focusing, Green's function retrieval, and their mutual relations, *Phys. Rev. Lett.*, **110**(8), 084301-1–084301-5.
- Wapenaar, K., Slob, E. & Snieder, R., 2010. On seismic interferometry, the generalized optical theorem and the scattering matrix of a point scatterer, *Geophysics*, **75**, SA27–SA35.
- Weglein, A., Gasparotto, F.A., Carvalho, P.M. & Stolt, R.H., 1997. An inverse-scattering series method for attenuating multiples in seismic reflection data, *Geophysics*, **62**, 1975–1989.